A Method to Reduce the Gibbs Ringing Artifact in MRI Scans While Keeping Tissue Boundary Integrity.

Rick Archibald and Anne Gelb

Abstract— **Gibbs ringing is a well known artifact that effects reconstruction of images having discontinuities. This is a problem in the reconstruction of magnetic resonance imaging (MRI) data due to the many different tissues normally present in each scan. The Gibbs ringing artifact manifests itself at the boundaries of the tissues, making it difficult to determine the structure of the brain tissue. The Gegenbauer reconstruction method has been shown to effectively eliminate the effects of Gibbs ringing in other applications. This paper presents the application of the Gegenbauer reconstruction method to neuro-imaging.**

Keywords— **Fourier reconstruction, Gibbs phenomenon, edge detection, Gegenbauer polynomials.**

I. Introduction

MAGNETIC resonance imaging (MRI) is a non-invasive procedure that provides discrete data about the human body. Information from an MRI scan is valuable for both clinical and research purposes. Large amounts of data are now available from MRI scans, giving computers a critical role in handling and interpreting the images produced. It is therefore imperative to develop accurate, efficient, and robust computer algorithms that can both reconstruct and segment images from MRI scans.

If the k-space data from the MRI is sampled rectilinearly, the filtered Fourier reconstruction method is commonly use to reconstruct the image [18]. Fourier approximation is a powerful tool in image reconstruction in the context of convergence, since an image having no discontinuities (or edges) has an exponentially and uniformly converging Fourier approximation to the original image. This superior convergence quality depends solely on the smoothness of the function. Unfortunately, however, if the image has discontinuities, then spurious oscillations will appear in the reconstruction at the discontinuities and the overall convergence rate will be greatly reduced. These spurious oscillations are called the Gibbs ringing artifact in magnetic resonance imaging, and are prevalent particularly at the tissue boundaries. Filters are often introduced to dampen the high frequency modes responsible for the oscillations and reduce the effects of Gibbs ringing. However, since important information about the finer features of an image is carried in the high frequency modes, filtering inevitably causes blurring of the features of the reconstructed image at the boundaries. This is a violation of the data-consistency constraint, but is tolerated in order to reduce the Gibbs ringing artifact [18].

The high resolution Gegenbauer reconstruction method requires the construction of a set of Gegenbauer coefficients from the k-space data of the MRI image, which is a computationally intensive procedure hindering large data calculations. The commonly used filtered Fourier reconstruction procedure is much more cost efficient because the fast Fourier transform (FFT) can be directly utilized. To maximize speed without compromising accuracy, we adopt the hybrid Gegenbauer procedure [7] that combines the highly resolved Gegenbauer reconstruction near the tissue boundaries with the computationally efficient filtered Fourier reconstruction away from the boundaries. A relationship between the Gegenbauer and Fourier coefficients [3] is also exploited to reduce computational cost.

This paper demonstrates the advantages of using the hybrid Gegenbauer reconstruction algorithm by comparing it to the commonly used filtered Fourier reconstruction on two different simulated brain phantoms. In §II the construction of the Shepp-Logan brain phantom is introduced. The Gibbs ringing artifact as a result of Fourier reconstruction is explained in §III. Filtering is presented in §IV as a possible remedy to the Gibbs ringing artifact. The edge detection method, critical in determining the smooth intervals for high resolution reconstruction, is explained in §V, followed by a discussion of the Gegenbauer reconstruction method in §VI, and the hybrid Gegenbauer approach in §VII. Finally, in §VIII we demonstrate the hybrid Gegenbauer reconstruction method for a realistic simulated brain phantom provide by McConnell Brain Imaging Centre Montréal Neurological Institute [16].

Throughout this paper we assume that all the data is unmodified, and note that in [1] the numerical algorithms introduced here were expanded to include reconstructing images that contain noise.

II. Shepp-Logan Brain Phantom

We introduce the commonly used Shepp-Logan brain phantom image in figure 1 to demonstrate the underlying principles of MRI reconstruction methods presented in this paper. This phantom represents a geometrically simplified magnetic resonance coronal scan of the head, and its algorithm is given in the appendix. Because of the sharp discontinuities present in the image, the phantom provides a basic model to test the effectiveness of different reconstruction methods in the context of neural imaging.

Arizona State University, Department of Mathematics, Tempe, Arizona 85287-1804, e-mail: rick@mathpost.la.asu.edu.

Arizona State University, Department of Mathematics, Tempe, Arizona 85287-1804, e-mail: ag@math.la.asu.edu.

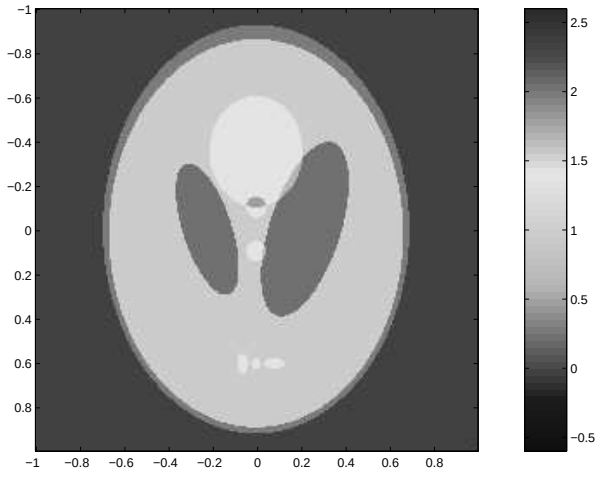

Fig. 1. The Shepp-Logan brain phantom image.

III. The Gibbs Ringing Artifact

Fourier approximation is frequently used for image reconstruction when discrete data is given on equally spaced points. As mentioned in the introduction, the error in the Fourier reconstruction of a function depends solely upon the smoothness of the function, since the decay rate of the Fourier coefficients is directly linked to the number of continuous derivatives of the function[13]. In the application of Fourier reconstruction to neural imaging, the underlying function has discontinuities at the tissue boundaries, and hence Gibbs ringing will be prevalent at the discontinuities with the overall rate of convergence reduced to first order.

To demonstrate the Gibbs ringing artifact, we consider the Fourier approximation of the following periodic function sampled on equally spaced discrete data points, $x_j = \frac{j-N}{N}, j = 0, \cdots, 2N-1$.

Example III.1: Let $f(x)$ be a piecewise smooth periodic function on $[-1, 1]$ defined by

$$f(x) = \begin{cases} -\cos(\frac{\pi x}{2}), & \text{if } -1 \le x \le -\frac{1}{2}, \\ 2 + \frac{\sin(6\pi x)}{3}, & \text{if } -\frac{1}{2} < x \le \frac{1}{2}, \\ 4x^3 + x^2 - 5x, & \text{if } \frac{1}{2} < x < 1. \end{cases} \quad (1)$$

The discrete data (pseudo-spectral) Fourier approximation is constructed as

$$f_N(x) = \sum_{k=-N}^{N} \tilde{f}_k e^{i\pi k x}, \quad (2)$$

where $\tilde{f}_k$ are the discrete Fourier coefficients computed from given discrete data $f(x_j)$ as

$$\tilde{f}_k = \frac{1}{2Nc_k} \sum_{j=0}^{2N-1} f(x_j) e^{-i\pi k x_j}, \qquad c_k = \begin{cases} 2, & \text{if } k = \pm N, \\ 1, & \text{otherwise.} \end{cases} \quad (3)$$

In practice, one uses the fast Fourier transform (FFT) subroutines to compute (2) and (3).

The graph of example III.1 and its Fourier approximation are shown in figure 2. The Gibbs ringing artifact is particularly evident at the discontinuities where there is an 18% overshoot and 18% undershoot.

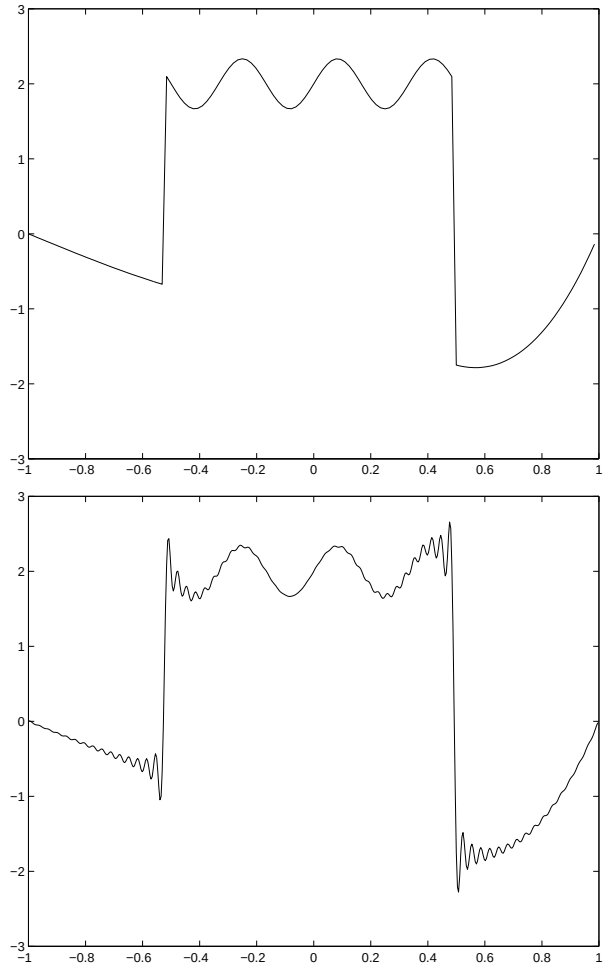

Fig. 2. (a) Piecewise Smooth function given in example III.1 and (b) Fourier reconstruction of the function on 128 points.

As an example of Fourier reconstruction in two dimensions, we consider the Shepp-Logan phantom image in figure 1 which is a piecewise smooth function on $[-1, 1] \times [-1, 1]$. The discontinuities are caused by the various tissues represented in the phantom. The Fourier approximation is computed as

$$f_N(x, y) = \sum_{k=-N}^{N} \sum_{l=-N}^{N} \tilde{f}_{k,l} e^{i\pi(kx+ly)}, \quad (4)$$

where the Fourier coefficients are recovered from the discrete data given on equally spaced points as

$$\tilde{f}_{k,l} = \frac{1}{4N^2 c_k c_l} \sum_{j=0}^{2N-1} \sum_{h=0}^{2N-1} f(x_j, y_h) e^{-i\pi(kx_j + ly_h)}. \quad (5)$$

The Gibbs ringing artifact is clearly evident in the Fourier reconstruction of the Shepp-Logan brain phantom exhibited in figure 3.

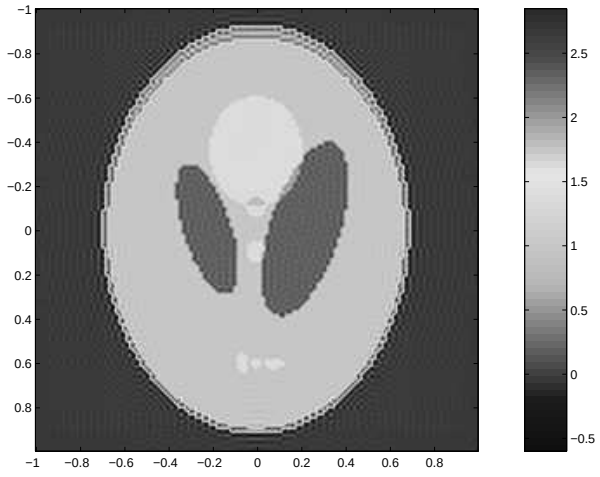

Fig. 3. Fourier Reconstruction of Shepp-Logan brain Phantom on $[128 \times 128]$ grid points.

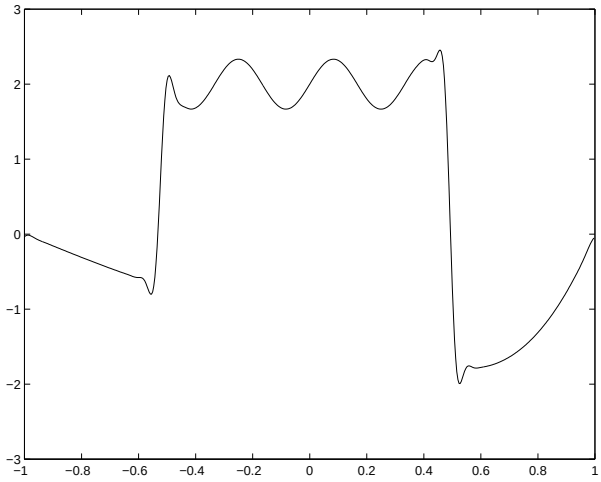

Fig. 4. Filtered Fourier reconstruction of example III.1 on 128 points with $p = 4$.

IV. Filtered Fourier Reconstruction

One factor contributing to the Gibbs ringing artifact for piecewise smooth functions is the slow decay rate of the Fourier expansion coefficients [13]. A filter increases the rate of decay by attenuating the higher order coefficients which in turn controls the effects of the Gibbs oscillations. The filtered discrete Fourier reconstruction in two dimensions is computed as

$$f_N^{\theta}(x,y) = \sum_{k=-N}^{N} \sum_{l=-N}^{N} \theta_k \theta_l \tilde{f}_{k,l} e^{i\pi(kx+ly)}, \qquad (6)$$

where $\theta_k = \theta(\frac{|k|}{N})$ is the exponential filter given by

$$\theta(\frac{|k|}{N}) = e^{-\alpha(\frac{|k|}{N})^p}. \qquad (7)$$

The exponential filter is one of many filters that can be used, and is chosen most often because of its high accuracy away from discontinuities, robustness, and simplicity. Other filters, e.g. Lanczos, raised cosine, etc., do not retain high accuracy away from the discontinuities. In (7) p represents the order of the filter and α measures the strength of the filter, generally chosen so that $\theta(1) \approx \mathcal{O}(\epsilon_m)$ where ϵ_m represents machine accuracy (Typically $\alpha = 32$). Figure 4 shows the filtered Fourier reconstruction of the piecewise smooth function in example III.1. The Gibbs ringing is indeed reduced, however the reconstruction is smeared at the discontinuities.

Filtered reconstructions of the Shepp-Logan brain phantom image are displayed in figures 5 and 6. Although the Gibbs ringing is alleviated by implementation of the exponential filter, and high accuracy is restored in the smooth regions away from the boundaries, the undesirable side effect of blurring the features at the boundaries is evident.

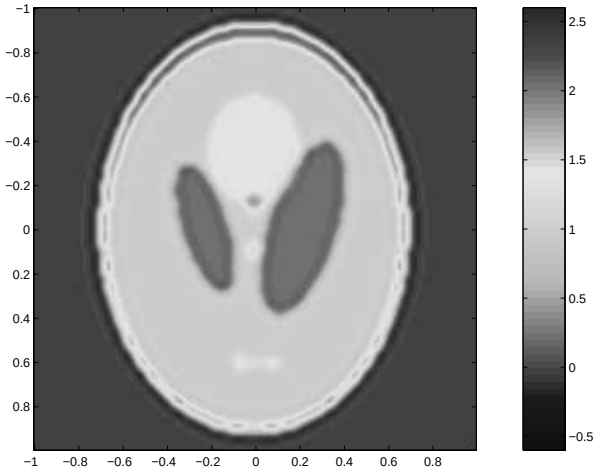

Fig. 5. Filtered Fourier reconstruction of the Shepp-Logan brain phantom on $[128 \times 128]$ equally space grid points.

V. Edge Detection

As mentioned in the introduction, detecting the edges of an image is the critical first step in a high resolution reconstruction. Information about the locations of the edges is used to determine the regions of smoothness in which the images can be reconstructed. Edge detection from spectral data has been the subject of many recent articles, and here we use the method developed in [9] which is summarized below.

Let us define the jump function $[f](x)$ for a piecewise smooth function as $[f](x) = f(x+) - f(x-)$, where $f(x\pm)$ are the right and left side limits of the function at x, $f(x\pm) = lim_{x \to x\pm} f(x)$. Note that $[f](x)$ is zero away from a discontinuity, and is the value of the jump at a discontinuity.

We choose a "concentration" kernel, K_N^{σ}, such that the support of $K_N^{\sigma} * f$ tends to the singular support, or jump discontinuities, of f. Specifically, we wish to "concentrate" at the discontinuities of $f(x)$ while tending to zero in the smooth regions, thus yielding the concentration property

$$K_N^{\sigma} * f(x) \longrightarrow [f](x), \qquad \text{as } N \longrightarrow \infty. \qquad (8)$$

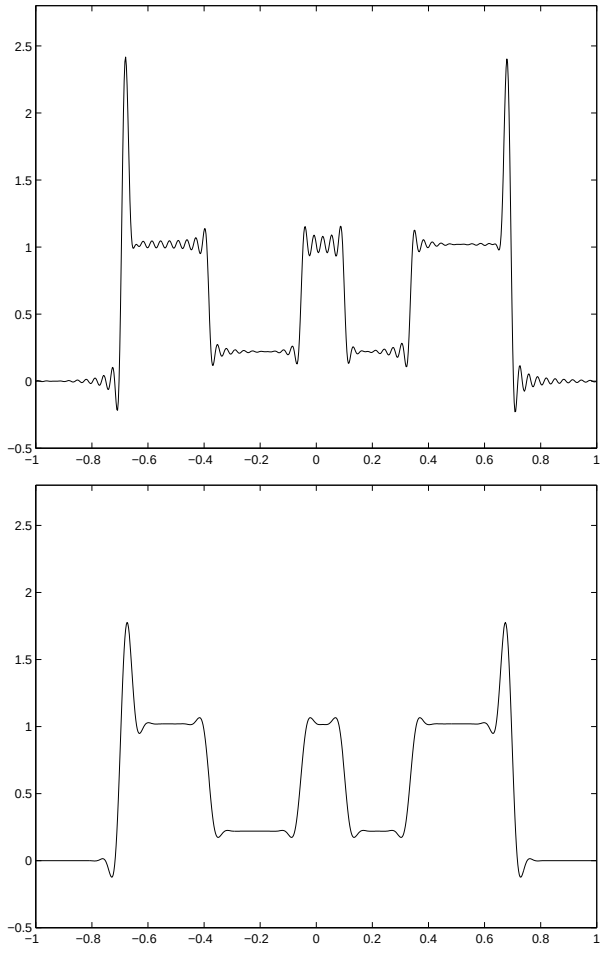

Fig. 6. (a) Fourier reconstruction and (b) filtered Fourier reconstruction on 128 points with $p = 4$ for a cross section of the Shepp-Logan Brain.

This "concentration" kernel is written as

$$K_N^\sigma(t) = -\sum_{k=1}^{N} \sigma(\frac{k}{N}) \sin kt,$$

where $\sigma(\frac{k}{N})$ are the concentration factors satisfying

$$\frac{\sigma(\xi)}{\xi} \in C^2(0,1).$$

It was shown in [9] that if the concentration factors $\sigma(\xi)$ are normalized so that

$$\int_0^1 \frac{\sigma(\xi)}{\xi} d\xi = 1,$$

then the concentration property (8) holds with the estimate

$$|K_N^\sigma * f(x) - [f](x)| \leq Const \cdot \frac{\log N}{N}.$$

The concentration method for detecting jump discontinuities is easily implemented as

$$K_N^\sigma * f(x) := S_N^\sigma[f](x) = i\pi \sum_{k=-N}^{N} sgn(k)\sigma(\frac{|k|}{N})\hat{f}_k e^{ik\pi x}, \tag{9}$$

where $\hat{f}_k$ are continuous Fourier coefficients and $\sigma(\frac{|k|}{N})$ are the concentration factors corresponding to the concentration kernel K_N^σ.

There are several examples of admissible concentration factors discussed in [9]. The exponential concentration factor, $\sigma(\xi) = Const \cdot \xi e^{\frac{1}{\alpha\xi(\xi-1)}}$, where $Const = \int_\epsilon^{1-\epsilon} exp(\frac{-1}{\alpha\eta(\eta-1)})d\eta$, is particularly effective, as it takes full advantage of the spectral data by rapidly converging away from the discontinuities. The parameter α is freely chosen, with a typical value $\alpha = 6$.

Since our information is based on discrete data points, we apply the analogous case for the discrete coefficients (3) which is implemented as

$$T_N^\tau[f](x) := i\pi \sum_{k=-N}^{N} sgn(k)\tau(\frac{|k|}{N+\frac{1}{2}})\tilde{f}_k e^{ik\pi x}, \tag{10}$$

where $\tilde{f}_k$ are the discrete Fourier coefficients (3), and the corresponding concentration factor $\tau(\xi)$ is given in [9] and [11] as

$$\tau(\xi) = \sigma(\xi)\frac{2\sin(\xi\pi)}{\xi\pi}. \tag{11}$$

The discrete case admits an analogous concentration property to (8) ensuring convergence of (10) to $[f](x)$, and is easily calculated with the FFT algorithm. We note that when the data given is k-space data, the edge detection method (9) can be directly applied. Let us recall example III.1, for which we wish to locate the discontinuities. Essentially, we wish to approximate the corresponding jump function,

$$[f](x) = \begin{cases} \frac{4+\sqrt{2}}{2}, & \text{if } x = -\frac{1}{2}, \\ -\frac{15}{4}, & \text{if } x = \frac{1}{2}, \\ 0, & \text{else.} \end{cases} \tag{12}$$

Figure 7 demonstrates the results of applying the concentration method to the piecewise smooth function in example III.1 where it is evident that (10) is converging to (or "concentrating" at) the positions and sizes of the discontinuities of the step function.

In order to determine the exact intervals of smoothness imperative for high resolution reconstruction, the concentration method (10) must be further enhanced to "pinpoint" the edges exactly. For this purpose, an edge enhancement procedure has been constructed in [10] and is described below.

The detection of edges is based on a separation of scales. More specifically, if $\{x_j^*\}_{j=1}^M$ denotes the locations of the jump discontinuities of $f(x)$, then for admissible concentration factors (11) we have

$$T_N^\tau[f](x) \to \begin{cases} [f](x_j^*), & \text{if } x = x_j^*, \\ \mathcal{O}(\frac{1}{N}), & \text{if } x \neq x_j^*. \end{cases}$$

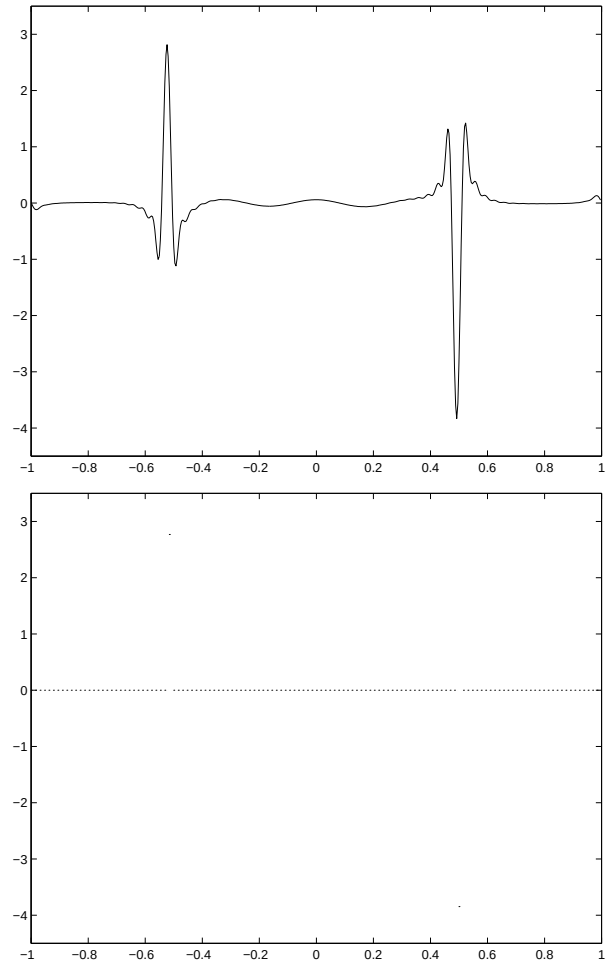

Fig. 7. (a) The jump function, and (b) the concentration method (10) on 128 points applied to the function in example III.1.

The nonlinear enhancement procedure [10] amplifies the separation of scales by computing

$$(T_N^\tau[f](x))^q \to \begin{cases} ([f](x_j^*))^q, & \text{if } x = x_j^*, \\ \mathcal{O}(\frac{1}{N})^q, & \text{if } x \neq x_j^*. \end{cases}$$

This separation of scales can be more pronounced by defining

$$E := N^{q/2}(T_N^\tau[f](x))^q \to \begin{cases} N^{q/2}([f](x_j^*))^q, & \text{if } x = x_j^*, \\ \mathcal{O}(N^{-q/2}), & \text{if } x \neq x_j^*, \end{cases}$$

leading to the enhanced edge detection method,

$$E_N(T_N^\tau[f](x)) = \begin{cases} T_N^\tau[f](x), & \text{if } |E| > J_{crit}, \\ 0, & \text{if } |E| < J_{crit}. \end{cases} \tag{13}$$

Here J_{crit} is an $\mathcal{O}(1)$ global threshold parameter signifying the minimal amplitude for the jump discontinuity not to be negligible. Since (10) actually locates the neighborhoods of the discontinuities, the exact jump locations are determined as the corresponding locations to the largest amplitudes $|E| > J_{crit}$ in each neighborhood of admissible jumps (i.e. where $|E| > J_{crit}$). Note that J_{crit} should be chosen to be consistent with the variation and scaling of the function. Experiments show that the parameter $q = 2$ is adequate for enhancement.

The nonlinear enhancement procedure works well when the discontinuities are located "far enough" from each other. (Experimentally the neighborhood of a discontinuity is approximately $5\Delta x$.) However when the discontinuities are extremely close together, as is the case of MRI scans, where two neighboring pixels may contain discontinuities, a more refined procedure near the locations of the discontinuities must be employed. The limitations of the nonlinear enhancement procedures in the case of MRI are exhibited in figure 8 and 19, where several jump locations are "missed".

To this end, we adopt a minimization procedure as explained in the following paragraphs.

We begin by defining the saw tooth function:

$$g(x; b_1) = \begin{cases} x + 1 & \text{if } -1 \leq x \leq b_1, \\ x - 1 & \text{if } b_1 < x \leq 1, \end{cases} \tag{14}$$

which is a periodic piecewise smooth function having a single jump discontinuity at $x = b_1$ with $[g](x; b_1) = -2$ for $x = b_1$ and $[g](x; b_1) = 0$ otherwise. The function $g(x; b_1)$ is easily extended to contain multiple discontinuities, $x = \{b_i\}_{i=1}^M$, as $[g](x; b) = \sum_{i=1}^M g(x, b_i)$.

If $f(x)$ is a periodic piecewise smooth function with discontinuities located at $x = \{b_i\}_{i=1}^M$ and corresponding jump values $[f](b_i) = a_i$, then

$$h(x) := f(x) + \sum_{i=1}^{M} \frac{a_i}{2} g(x; b_i) \tag{15}$$

defines a smooth and periodic function. Clearly the jump function $[h](x) = [f](x) + \sum_{i=1}^M \frac{a_i}{2}[g](x; b_i) = 0$, and by the concentration property, $T_N^\tau[h](x)$ converges to $[h](x)$, setting up the minimization problem,

$$\begin{aligned} \min_{M, a_i, b_i} \max_x |T_N^\tau[h](x)| \quad := \quad & \min_{M, a_i, b_i} \max_x |T_N^\tau[f](x) \\ + \quad & \sum_{i=1}^{M} \frac{a_i}{2} T_N^\tau[g](x; b_i)|, \end{aligned} \tag{16}$$

to yield the size and positions of the jump discontinuities of $f(x)$. Here b_i and a_i, $i = 1, \cdots, M$, are the positions and corresponding jump values of the discontinuities, and M is the total number of discontinuities. We note that the choice of (14) is not unique, but it is chosen because of its simplicity. There may be advantages in choosing other functions.

This method of minimization provides an interesting optimization problem. By the concentration property (10), since $\max_x |T_N^\tau[f](x)|$ converges to the height of the largest

discontinuity of f, one can then conclude that

$$\begin{aligned}\max_x |T_N^\tau[h](x)| &= \max_x |T_N^\tau[f](x) + \sum_{i=1}^{M} \frac{a_i}{2} T_N^\tau[g](x;b_i)| \\ &\to 0. \end{aligned} \quad (17)$$

The problem can now be formulated as follows. If M, a_i, and b_i are correctly chosen for $i = 1, \cdots, M$ then

$$\max_x |T_N^\tau[h](x)| < \mathcal{O}(\frac{1}{N}). \quad (18)$$

The correct choice of M, a_i, and b_i therefore gives the unique minimum of (16) within a pixel distance.

The minimization procedure for (16) lacks refinement. If all possible values of M, a_i, and b_i are numerically calculated, uniqueness of (16) ensures their correct values. Unfortunately, such a procedure is extremely costly computationally.

Since the nonlinear enhancement procedure (13) is very efficient for discontinuities that are not close together, we can apply this procedure first to locate the discontinuities that are not close together (e.g. a distance greater than $5\Delta x$). After isolated discontinuities are found, the remaining discontinuities can be found through numerical calculation of (16). The proposed combination procedure takes advantage of both the speed of the nonlinear enhancement (13) and the accuracy of the numerical minimization (16).

To simplify notation we combine the set of jump locations and jump sizes into a set of ordered pairs,

$$\mathbf{D} = \left\{ \mathbf{b_i}, \mathbf{a_i} = [\mathbf{f}](\mathbf{b_i}) \right\}_{\mathbf{i=1}}^{\mathbf{M}}. \quad (19)$$

The following algorithm converges to the set $\mathbf{D}$:

Algorithm V.1: (Algorithm used to determine the set $\mathbf{D}$, which is the set of jump discontinuities $\{b_i\}_{i=1}^{M}$ and their corresponding set of jump values $\{a_i\}_{i=1}^{M}$, for any piecewise smooth periodic function $f(x)$ on $[-1, 1]$.)

1. The concentration method (9) and nonlinear enhancement procedure (13) are performed. Then for the set of grid point values $\{x_j = \frac{j-N}{N}\}_{j=0}^{2N-1}$, we determine an initial set of discontinuities

$$\mathbf{D_1} = \left\{ \mathbf{b_{1,i}}, \mathbf{a_{1,i}} = [\mathbf{f}](\mathbf{b_{1,i}}) \right\}_{\mathbf{i=1}}^{\mathbf{M_1}}. \quad (20)$$

Here $b_{1,i}$ are the discontinuity points "pinpointed" after the nonlinear enhancement procedure, $a_{1,i}$ are their corresponding jump values, and M_1 is the total number of discontinuities. Specifically, in (13) when $E_N(T_N^\tau[f](x_j)) > 0$, we have $b_{1,i} = x_j$, $a_{1,i} = E_N(T_N^\tau[f](b_{1,i}))$, and M_1 is the total number of nonzero values for $E_N(T_N^\tau[f](x_j))$, $j = 0, \cdots, 2N-1$.

2. We can determine the discontinuities that are missing from $\mathbf{D_1}$ by applying the procedure described in (17) with $b_{1,i}$ and $a_{1,i}$, $i = 1, \cdots, M_1$, as the respective discontinuity points and jump values. Hence for $j = 0, \cdots 2N-1$, we use (9) and (13) to compute

$$E_N(T_N[h](x_j)) = E_N\Big(T_N[f](x_j) - \sum_{i=1}^{M_1} (\frac{a_{1,i}}{2} T_N^\tau[g](x_j;b_{1,i}))\Big). \quad (21)$$

Then the set of missed discontinuities,

$$\mathbf{D_2} = \left\{ \mathbf{b_{2,i}}, \mathbf{a_{2,i}} = [\mathbf{f}](\mathbf{b_{2,i}}) \right\}_{\mathbf{i=1}}^{\mathbf{M_2}}, \quad (22)$$

consists of $b_{2,i} = x_i$ and $a_{2,i} = E_N(T_N[h](b_{2,i})) > 0$. Here M_2 is the total number of nonzero values of $E_N(T_N[h](x_j))$.

3. The set of discontinuities is updated by augmenting it with the set of missed discontinuities as

$$\mathbf{D_1} = \mathbf{D_1} \cup \mathbf{D_2}. \quad (23)$$

We note that it is possible that some ordered pairs in this new set $\mathbf{D_1}$ may have the same discontinuity location but different jump values, i.e. $b_{1,i} = b_{2,j}$ but $a_{1,i} \neq a_{2,j}$ for some integer values $i \in [1, M_1]$ and $j \in [1, M_2]$. This occurs when a jump value is not computed accurately enough and is "corrected" in $\mathbf{D_2}$, often as a result of jump locations occurring only a few pixels apart. At this point, in the new set $\mathbf{D_1}$ we assign the jump discontinuity, $b_{1,i}$, the corresponding jump value $a_{1,i} = a_{1,i} - a_{2,j}$.

4. The above two steps are repeated until $\mathbf{D_2}$ yields the empty set, leaving $\mathbf{D} = \mathbf{D_1}$. □

We note that although for computational simplicity we assumed discontinuity locations will occur only on grid points, the edge detection procedure is not restricted in this way. Convergence of this algorithm is rapid, taking fewer than ten iterations for each example used in this paper.

The boundary detection method and minimization process can be extended to detect the size and position of discontinuities in a two dimensional function by holding each dimension fixed and determining the edges as a function of the fixed coordinate. Specifically, the concentration method for the discrete case in two dimensions is

$$\begin{aligned} T_N[f](x(\bar{y})) &= i\pi \sum_{k=-N}^{N} sgn(k)\tau(\frac{|k|}{N+\frac{1}{2}}) \\ &\quad \cdot \sum_{l=-N}^{N} \tilde{f}_{k,l} e^{(i\pi(kx+l\bar{y}))} \end{aligned} \quad (24)$$

$$\begin{aligned} T_N[f](y(\bar{x})) &= i\pi \sum_{l=-N}^{N} sgn(l)\tau(\frac{|l|}{N+\frac{1}{2}}) \\ &\quad \cdot \sum_{k=-N}^{N} \tilde{f}_{k,l} e^{(i\pi(k\bar{x}+ly))} \end{aligned} \quad (25)$$

where $\bar{x}$ and $\bar{y}$ are fixed coordinates. We apply the exponential concentration factor given in (11). Figure 8 demonstrates the concentration method applied to the cross section $f(x, 0)$ of the Shepp-Logan brain phantom. After applying the nonlinear enhancement and minimization procedures, it is possible to detect the location of the discontinuities between different tissues as well as the size of the jump discontinuities. Figure 9 exhibits the final boundary detection of the Shepp-Logan brain phantom using the

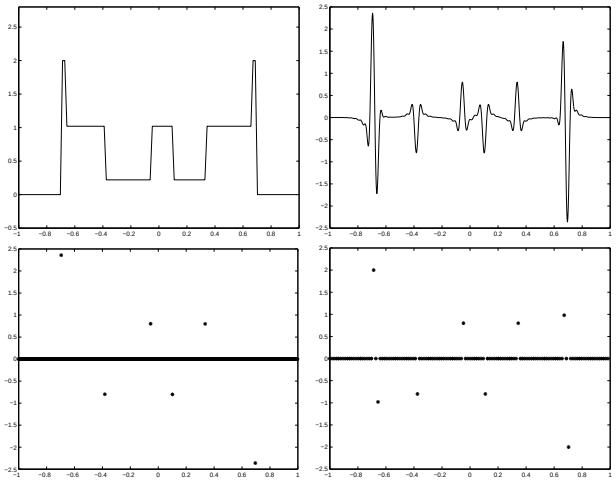

Fig. 8. (a) The cross section $f(x,0)$ of the Shepp-Logan phantom brain, (b) the concentration method applied on 128 points, (c) nonlinear enhancement of the concentration method, and (d) the minimization algorithm results.

minimization procedure in both directions. It should be noted that the x-direction and y-direction boundary detection provide overlapping information, with the most reliable information occurring when the boundary is perpendicular to the direction of detection.

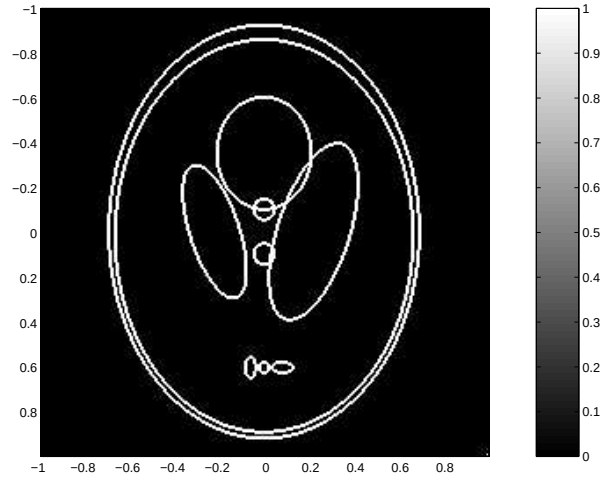

Fig. 9. Final boundary detection of the Shepp-Logan brain phantom for a $[128 \times 128]$ grid.

VI. The Gegenbauer Reconstruction Method

The Gegenbauer reconstruction method was developed in [15] and extended in a litany of articles (consult [14] for references). It is a powerful tool that recovers piecewise smooth functions with spectral accuracy *up to* the edges in each smooth interval, and can therefore be used to completely eliminate the Gibbs ringing artifact without compromising high resolution at the edges. Let us first introduce the Gegenbauer reconstruction method for a smooth function $f(x)$ on $[-1,1]$.

The Gegenbauer polynomial $C_n^\lambda(x)$ is an orthogonal polynomial of order n that satisfies

$$\int_{-1}^{1}(1-x^2)^{\lambda-\frac{1}{2}}C_k^\lambda(x)C_n^\lambda(x)dx = \begin{cases} h_n^\lambda, & k=n, \\ 0, & k\neq n, \end{cases} \tag{26}$$

where (for $\lambda \geq 0$)

$$h_n^\lambda = \frac{\sqrt{\pi}C_n^\lambda(1)\Gamma(\lambda+\frac{1}{2})}{\Gamma(\lambda)(n+\lambda)}, \tag{27}$$

with

$$C_n^\lambda(1) = \frac{\Gamma(n+2\lambda)}{n!\Gamma(2\lambda)}. \tag{28}$$

An L_1-bounded function $f(x)$ on $[-1,1]$ can be represented by the Gegenbauer series expansion

$$f(x) = \sum_{l=0}^{\infty}\hat{f}^\lambda(l)C_l^\lambda(x), \tag{29}$$

where the spectral Gegenbauer coefficients are defined by

$$\hat{f}^\lambda(l) = \frac{1}{h_l^\lambda}\int_{-1}^{1}(1-x^2)^{\lambda-\frac{1}{2}}f(x)C_l^\lambda(x)dx. \tag{30}$$

We note that the Gegenbauer polynomials are related to the more commonly used associated Legendre polynomials by [3]

$$C_n^\lambda(x) = \frac{\Gamma(\lambda+\frac{1}{2})\Gamma(2\lambda+n)}{n!\Gamma(2\lambda)}\left[\frac{1}{4}(x^2-1)\right]^{\frac{1}{4}-\frac{\lambda}{2}}P_{n+\lambda-1}^{\frac{1}{2}-\lambda}(x).$$

Since the Gegenbauer polynomials are orthogonal, the partial Gegenbauer sum,

$$f_m^\lambda(x) = \sum_{l=0}^{m}\hat{f}^\lambda(l)C_l^\lambda(x), \tag{31}$$

converges exponentially to the smooth function $f(x)$ in $[-1,1]$.

In general, (30) must be evaluated using an approximation of $f(x)$. In the case where images are to be reconstructed from (discrete) spectral Fourier data (e.g. in the case of MRI reconstruction where we have k-space data), it was shown in [15] that the truncated Fourier expansion $f_N(x)$ in (2) can be used to approximate (30) for each $l = 0, \cdots, m$ as

$$\tilde{g}^\lambda(l) = \frac{1}{h_l^\lambda}\int_{-1}^{1}(1-x^2)^{\lambda-\frac{1}{2}}f_N(x)C_l^\lambda(x)dx. \tag{32}$$

The approximation is exponentially accurate provided that $\lambda, m \sim N$. In turn (31) is approximated by

$$g_m^\lambda(x) = \sum_{l=0}^{m}\tilde{g}^\lambda(l)C_l^\lambda(x), \tag{33}$$

where it was again shown in [15] that the approximation is exponentially accurate for smooth (non-periodic) functions on $[-1,1]$ as long as $\lambda, m \sim N$. We recall that the

regular Fourier reconstruction (2) applied to a smooth but non-periodic function will produce Gibbs oscillations at the boundaries and an overall reduced convergence rate of $\mathcal{O}(\frac{1}{N})$. Conversely, the filtered Fourier reconstruction (6) for a smooth but non-periodic function will alleviate these oscillations but cause blurring at the boundaries. Hence we see that the poorly performing Fourier approximation can be turned into an exponentially converging Gegenbauer approximation via (32) and (33) even up to the boundaries. To efficiently compute the Gegenbauer approximation (33), we exploit the relationship in [3],

$$\frac{1}{h_l^\lambda}\int_{-1}^{1}(1-x^2)^{\lambda-\frac{1}{2}}e^{in\pi x}C_l^\lambda(x)dx = \Gamma(\lambda)(\frac{2}{\pi n})^\lambda i^l(l+\lambda)J_{l+\lambda}(\pi n), \tag{34}$$

where $J_\nu(x)$ is the Bessel function. This formula, together with the discrete Fourier coefficients (3), provides the explicit expression for the approximate Gegenbauer coefficients (32) as

$$\tilde{g}^\lambda(l) = \delta_{0l}\hat{f}(0) + \Gamma(\lambda)i^l(l+\lambda)\sum_{0<|k|\le N} J_{l+\lambda}(\pi k)(\frac{2}{\pi k})^\lambda \tilde{f}(k). \tag{35}$$

In this form, FFT techniques can be employed in the calculation of the Gegenbauer coefficients.

The Gegenbauer reconstruction method can be similarly performed when $f(x)$ is smooth in any arbitrary interval $[a,b]$. Specifically, let us define a local variable $\eta \in [-1,1]$ such that $x(\eta) = \epsilon\eta + \delta$, where $\epsilon = \frac{b-a}{2}$ and $\delta = \frac{b+a}{2}$. The Gegenbauer reconstruction is then based on the Fourier approximation of $f(x)$ in $[a,b]$,

$$f_N(x(\eta)) = f_N(\epsilon\eta+\delta) = \sum_{k=-N}^{N}\tilde{f}_k e^{ik\pi(\epsilon\eta+\delta)}, \tag{36}$$

and is computed by

$$g_m^\lambda(x(\eta)) = \sum_{l=0}^{m}\tilde{g}_\epsilon^\lambda(l)C_l^\lambda(\eta), \tag{37}$$

where the approximate Gegenbauer coefficients,

$$\tilde{g}_\epsilon^\lambda(l) = \frac{1}{h_l^\lambda}\int_{-1}^{1}(1-\eta^2)^{\lambda-\frac{1}{2}}f_N(x(\eta))C_l^\lambda(\eta)d\eta, \tag{38}$$

are computed by the FFT algorithm as

$$\tilde{g}_\epsilon^\lambda(l) = \delta_{0l}\hat{f}(0) + \Gamma(\lambda)i^l(l+\lambda) \cdot \sum_{0<|k|\le N} J_{l+\lambda}(\pi k\epsilon)(\frac{2}{\pi k\epsilon})^\lambda e^{ik\pi\delta}\hat{f}(k). \tag{39}$$

Figure 10 shows the Gegenbauer reconstruction of the piecewise smooth function of example III.1. The method is applied in each smooth subinterval and then the three reconstructed regions are "glued" together to form the final

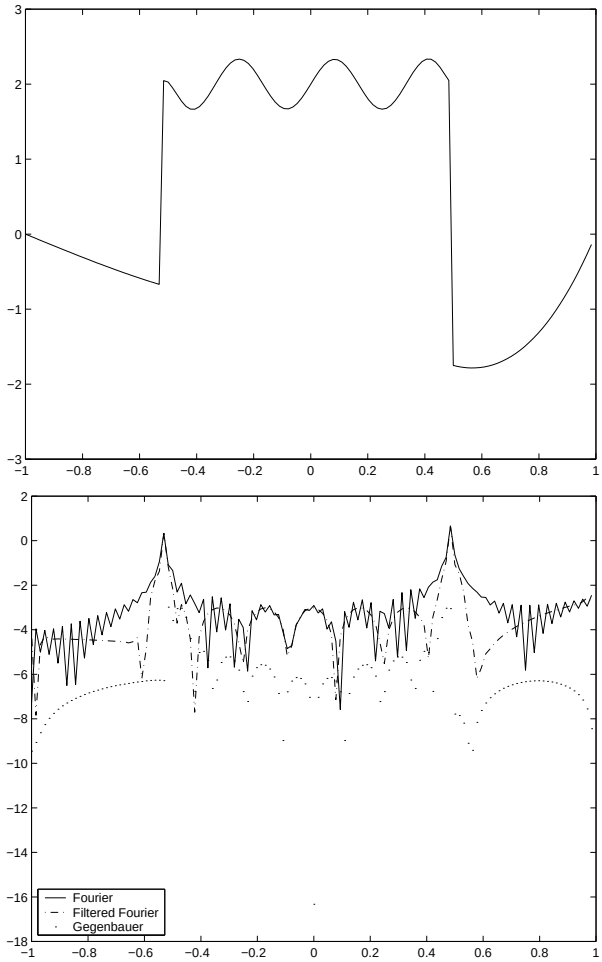

Fig. 10. (a) Gegenbauer reconstruction of example III.1 on $[-1,1]$, with $2N = 128$, $m = 8$, and $\lambda = 4$. (b) Log of the error for Fourier, filtered Fourier, and Gegenbauer reconstruction.

approximation. Figure 11 depicts the clear improvement of applying the Gegenbauer reconstruction method over the filtered Fourier approximation (figure 6) to a cross section of the Shepp-Logan phantom. The intervals of smoothness are found first by the edge detection method described in §V, and then Gegenbauer reconstruction is performed in each smooth interval up to the edges of each interval. As is evident from the figure, there are some smooth intervals consisting of too few points to construct an approximation. (Gegenbauer reconstruction requires at least a theoretical minimum of π points to form an approximation [13].) In these intervals, the values at each grid point are assumed constant and equivalent to the values determined at the edges. The procedure is further described in §VII. Figure 12(b) shows the resulting error of the Gegenbauer reconstruction method for the Shepp-Logan phantom, where it is evident that a high rate of convergence is obtained. No optimization of parameters was attempted, and the method works as a black box.

The Gegenbauer reconstruction method is of $\mathcal{O}(10^d)$ times computationally slower then Fourier or filtered Fourier reconstruction, where d is the dimension of the

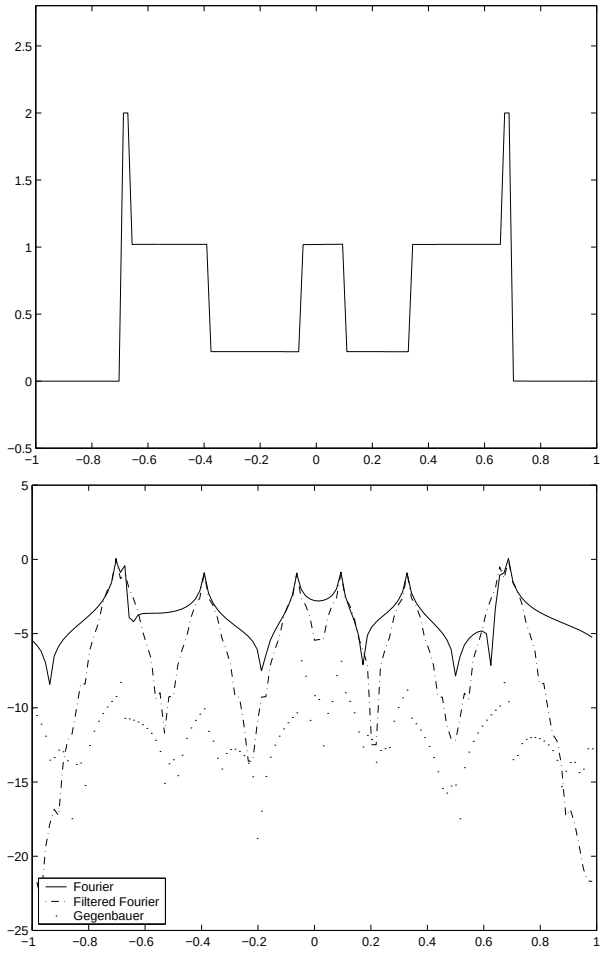

Fig. 11. (a) Gegenbauer reconstruction applied to the Shepp-Logan phantom at the cross section $(x, 0)$. Here $2N = 128$, $m = 4$, and $\lambda = 4$. (b) Log of the error for Fourier, filtered Fourier, and Gegenbauer reconstruction.

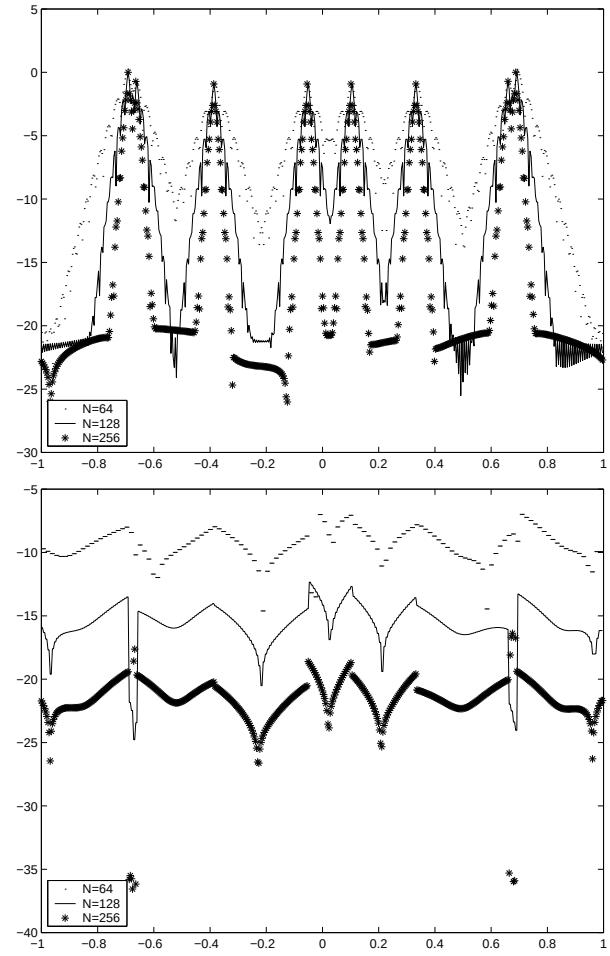

Fig. 12. Log of the absolute error in (a) filtered reconstruction, and (b) Gegenbauer reconstruction of the Shepp Logan phantom at the cross section $(x, 0)$ for $N = 64, 128, 252$.

function. It is possible to reduce the computational time of the Gegenbauer method by reducing the number of pixel points values that are reconstructed using this method. Since the Gegenbauer reconstruction has a significant reduction in error close to the edges, it is critical to employ it in those regions. However, as exhibited in figures 11 and 12, the filtered Fourier reconstruction is effective in regions away from the discontinuities. That being said, the next section describes a method that takes advantage of the computational efficiency of filtered Fourier reconstruction in regions away from the discontinuities, while assuring the high resolution of the Gegenbauer reconstruction method near the edges.

VII. The Hybrid Reconstruction Method

The Gegenbauer reconstruction method is clearly superior to exponential filtering in terms of its high resolution reconstruction capabilities up to the edges of each smooth subinterval. However, it is considerably more computationally costly than the filtered Fourier reconstruction. Although the filtered Fourier reconstruction suffers from smeared resolution at the boundaries, it retains high accuracy in the smooth regions away from the edges. The hybrid method, developed in [7], takes advantage of the strengths of both methods in applying Gegenbauer reconstruction near the tissue boundaries and the filtered Fourier reconstruction away from the tissue boundaries.

For example, let us consider a piecewise smooth function $f(x)$ that is continuous inside the interval $[a, b]$. Then the hybrid method is given as

$$g_m^{\theta,\lambda}(x) = \begin{cases} g_m^{\lambda}(x), & \text{if } a \le x \le a+\rho \\ & \text{or } b-\rho \le x \le b, \\ f_N^{\theta}(x), & \text{if } a+\rho < x < b-\rho, \end{cases} \tag{40}$$

where $f_N^{\theta}(x)$ is the one-dimensional version of (6), and $0 \le \rho \le \frac{b-a}{2}$ is a neighborhood parameter. Clearly larger ρ implies greater accuracy, since the Gegenbauer reconstruction method would be applied in a greater interval. On the other hand, a smaller value for ρ yields reduced computational cost.

Now let us consider the two dimensional piecewise smooth function $f(x, y)$ continuous inside the interval $a_x \le x \le b_x$, $a_y \le y \le b_y$. Also, let XBP and YBP stand for

the closest edges of the smooth subinterval, a_x or b_x and a_y or b_y respectively. We define the hybrid method to be performed in each smooth subinterval $x \in [a_x, b_x], y \in [a_y, b_y]$ as

$$g_m^{\theta,\lambda}(x,y) = \begin{cases} \sum_{k=-N}^{N}\sum_{l=-N}^{N} \theta_k\theta_l \tilde{f}_{k,l} e^{i\pi(kx+ly)}, \\ \text{if } |x-XBP| \geq \rho \text{ and } |y-YBP| \geq \rho, \\ \\ \sum_{k=-N}^{N}\sum_{l=0}^{m} \theta_k A_{l,k} C_l^\lambda(x) e^{i\pi ky}, \\ \text{if } |x-XBP| < \rho \text{ and } |y-YBP| \geq \rho, \\ \\ \sum_{k=-N}^{N}\sum_{l=0}^{m} \theta_k B_{k,l} C_l^\lambda(y) e^{i\pi kx}, \\ \text{if } |x-XBP| \geq \rho \text{ and } |y-YBP| < \rho, \\ \\ \sum_{k=0}^{m}\sum_{l=0}^{m} \tilde{g}_{k,l}^\lambda C_k^\lambda(x) C_l^\lambda(y), \\ \text{if } |x-XBP| < \rho \text{ and } |y-YBP| < \rho. \end{cases} \tag{41}$$

The hybrid method (41) is defined so that the method of reconstruction for $f(x,y)$ is chosen based on the proximity to the nearest boundary in each direction. Specifically, the high resolution Gegenbauer reconstruction is chosen in close proximity to the edges of the smooth interval, and the more cost efficient exponential filtering is appropriately chosen everywhere else. For example, if Gegenbauer reconstruction is to be performed in the x direction with filtering in the y direction, we have

$$g_m^{\theta,\lambda}(x,y) = \sum_{l=0}^{m}\sum_{k=-N}^{N} \theta_k A_{l,k} C_l^\lambda(x) e^{i\pi ky}, \tag{42}$$

where the coefficients $A_{l,k}$ are given by

$$\begin{aligned} A_{l,k} &= \sum_{j=-N}^{N} \Big(\delta_{0l}\tilde{f}_{0,k} + \Gamma(\lambda) i^l (l+\lambda) \\ &\cdot \sum_{0<|\nu|\leq N} J_{l+\lambda}(\pi\nu)\Big(\frac{2}{\pi\nu}\Big)^\lambda \tilde{f}_{\nu,k}\Big) e^{-i\pi k y_j}. \end{aligned} \tag{43}$$

Similarly, if Gegenbauer reconstruction is chosen for the y direction with exponential filtering in the x direction, we have

$$g_m^{\theta,\lambda}(x,y) = \sum_{l=0}^{m}\sum_{k=-N}^{N} \theta_k B_{k,l} C_l^\lambda(y) e^{i\pi kx}, \tag{44}$$

for the coefficients

$$\begin{aligned} B_{k,l} &= \sum_{j=-N}^{N} \Big(\delta_{0l}\tilde{f}_{k,0} + \Gamma(\lambda) i^l (l+\lambda) \\ &\cdot \sum_{0<|\nu|\leq N} J_{l+\lambda}(\pi\nu)\Big(\frac{2}{\pi\nu}\Big)^\lambda \tilde{f}_{k,\nu}\Big) e^{-i\pi k x_j}. \end{aligned} \tag{45}$$

If both x and y are close to the edges of the interval, then we apply the Gegenbauer reconstruction procedure in both directions. The approximate Gegenbauer coefficients in two dimensions are a direct extension of (32),

$$\begin{aligned} \tilde{g}_{k,l}^\lambda &= \frac{1}{h_k^\lambda h_l^\lambda}\int_{-1}^{1}\int_{-1}^{1} (1-\eta_x^2)^{\lambda-\frac{1}{2}}(1-\eta_y^2)^{\lambda-\frac{1}{2}} \\ &\cdot f_N(x(\eta_x)y(\eta_y)) C_k^\lambda(\eta_x) C_l^\lambda(\eta_y) d\eta_x d\eta_y, \end{aligned} \tag{46}$$

where η_x and η_y are the local variables in $[-1,1]$ defined by $x(\eta_x) = \epsilon_x\eta_x + \delta_x$ and $y(\eta_y) = \epsilon_y\eta_y + \delta_y$ with $\epsilon_x = \frac{1}{2}(b_x - a_x)$, $\epsilon_y = \frac{1}{2}(b_y - a_y)$, $\delta_x = \frac{1}{2}(b_x + a_x)$, and $\delta_y = \frac{1}{2}(b_y + a_y)$. The Gegenbauer coefficients approximation is based on the two dimensional Fourier partial sum $f_N(x(\eta_x), y(\eta_y))$ computed in (36). We note that although the Gegenbauer parameters can assume different values in each direction, for simplicity we choose $\lambda = \lambda_x = \lambda_y$ and $m = m_x = m_y$. Our approximation using the Gegenbauer reconstruction method in both directions is then

$$g_m^{\theta,\lambda}(x,y) = \sum_{k=0}^{m}\sum_{l=0}^{m} \tilde{g}_{k,l}^\lambda C_k^\lambda(x) C_l^\lambda(y). \tag{47}$$

We have now acquired all of the necessary tools for the reconstruction of piecewise smooth data. The following procedure is implemented as a black box once the initial parameters are chosen, and is easily extended to higher dimensions:

Algorithm VII.1: (Algorithm used to reconstruct piecewise smooth function $f(x)$ on $[-1,1]$ using the edge detection and the hybrid Gegenbauer reconstruction procedures.)

1. Construct the Fourier coefficients from the grid point data (2). Note that this step is eliminated when the $k-$space data is given directly.
2. Apply algorithm V.1 to locate the discontinuities and their corresponding jump values.
3. After choosing Gegenbauer parameters m and λ in (33), filter order p (7), and hybrid neighborhood parameter ρ (40), apply the hybrid Gegenbauer method (41) to reconstruct the image inside each smooth interval containing enough resolution.
4. Using the jump values obtained from the edge detection and minimization procedures, the values at the edges of each smooth interval can be approximated by summing the Gegenbauer approximation of the neighboring point and the jump discontinuity height at the edge. This is accomplished for each smooth subinterval $[a,b]$ by computing

$$\begin{aligned} g_m^{\theta,\lambda}(a) &= g_m^{\theta,\lambda}(a-\Delta x) + [f](a), \\ g_m^{\theta,\lambda}(b) &= g_m^{\theta,\lambda}(b+\Delta x) + [f](b), \end{aligned} \tag{48}$$

In fact, the Gegenbauer method recovers $f(x)$ right up to the discontinuity and this step is not required. However, we have found that applying (48) is useful if the discrete function image has discontinuity points that are assumed to occur *on* the actual data points, as we have assumed here.

5. For "small" smooth intervals, i.e. $|b-a| \leq 4\Delta x$ where $\Delta x = \frac{1}{N}$ is the grid size, the values at the edges are determined by (48) and then each grid point value in (a,b) is assumed constant, either $g_m^{\theta,\lambda}(x) = g_m^{\lambda}(a)$ or $g_m^{\theta,\lambda}(x) = g_m^{\lambda}(b)$ for $x \in (a,b)$. We note that other interpolation procedures (e.g. linear) can be performed, but in general the variation in these intervals is so small that constant interpolation is adequate. □

For the Shepp-Logan brain phantom reconstruction, we apply the procedure described above to each pixel with $\rho = 5\Delta x$, $m = \lambda = 4$ and $p = 4$. We choose λ, m small since the image has little texture, as demonstrated in example III.1. The Gegenbauer reconstruction method is capable of reproducing images with more texture by using greater values for λ and m. Although larger λ and m would work here as well, the cost of computation is eased by smaller values.

Figure 13 depicts the filtered reconstruction of the phantom away from the boundaries, and figure 14 shows the reconstructed regions close to the boundaries using the two dimensional Gegenbauer method in regions where there is enough resolution to perform Gegenbauer reconstruction. These two figures constitute the hybrid reconstruction method (41). In the last step, boundary information determined by the edge detection procedure is added, and constant interpolation is performed in the very small intervals. The completely reconstructed image is seen in figure 15, where its enormous improvement over the traditional imaging technique of filtered Fourier reconstruction is evident. The overall computational time is of the same order as Fourier reconstruction. The discrepancies visible in figure 15 result from the interface matching of filtered Fourier reconstruction and Gegenbauer reconstruction. If one wishes to further improve the accuracy of reconstruction, the Gegenbauer method should be used for larger intervals, which will increase the cost of computation.

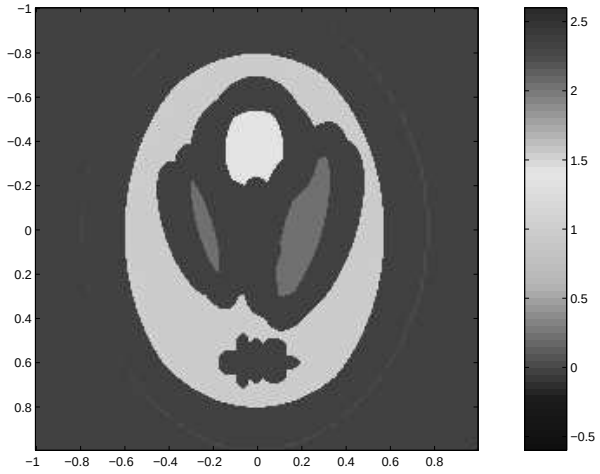

Fig. 13. Filtered Fourier reconstruction with $p = 4$ away from boundaries.

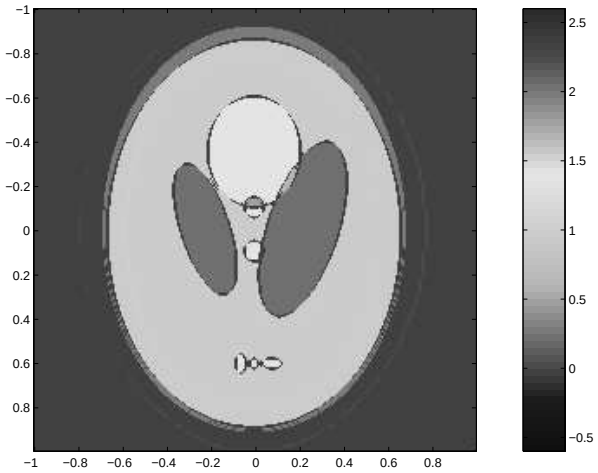

Fig. 14. Gegenbauer reconstruction with $m = \lambda = 4$ applied to large enough intervals near the boundaries.

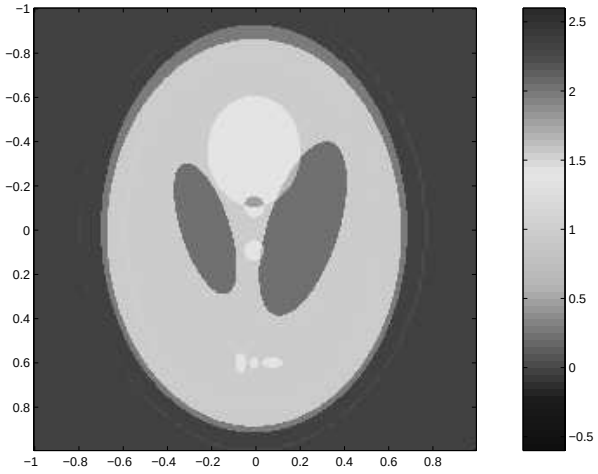

Fig. 15. Information about boundaries and constant interpolation is performed in very small intervals of smoothness to achieve the final hybrid Gegenbauer reconstruction of the simulated brain phantom.

VIII. The Simulated Brain Phantom

As our second example of an MRI phantom, we use the digital phantom provided by the McConnell Brain Imaging Centre Montréal Neurological Institute, [4], [5], [16], and [17]. This is a more realistic representation of a T1 weighted magnetic resonance coronal scan of the head, as can be seen in figure 16, where greater complexity than in the Shepp-Logan brain phantom is evident. The phantom does not present a clear image because of the coarse grid of available sample points.

Table 1 shows the intensities that were assigned to each tissue type in the simulated brain phantom.

The filtered Fourier reconstruction of the simulated brain phantom is shown in figure 17. Reconstruction is performed on a grid double the size of the original phantom to rectify the "graininess" of the image. The traditional method of image reconstruction clearly blurs the image, which is a direct result from applying the filter.

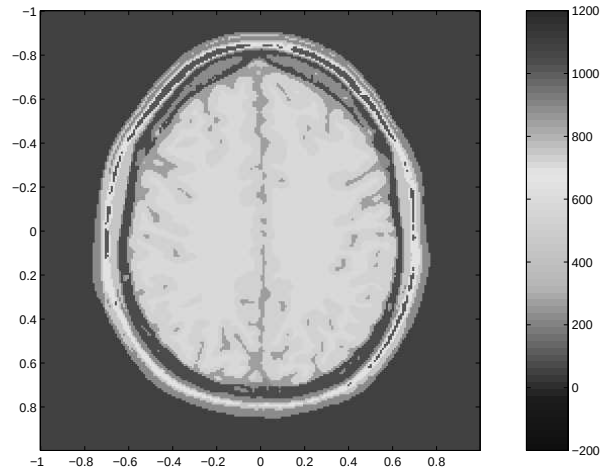

Fig. 16. Simulated digital brain phantom on a $[218 \times 218]$ grid.

TABLE I
INTENSITY ASSIGNED TO EACH TISSUE TYPE IN THE SIMULATED BRAIN PHANTOM.

Tissue	Intensity
Background	50
CSF	280
Grey matter	540
White matter	730
Fat	1030
Muscle/Skin	460
Skin	240
Skull	85
Connective	710

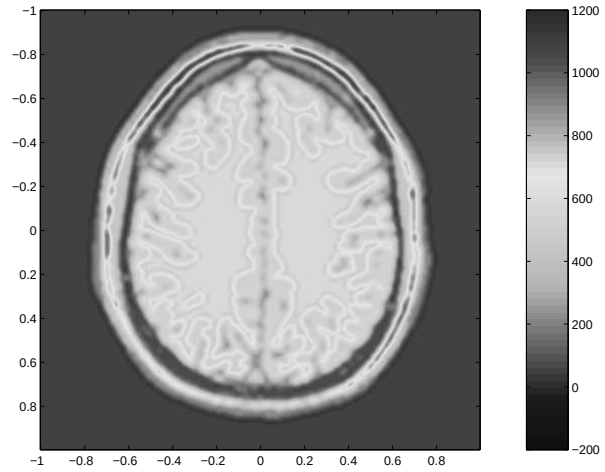

Fig. 17. Filtered Fourier reconstruction of the simulated brain phantom on a $[218 \times 218]$ grid with filter order $p = 4$.

Figure 18 displays an x-axis cross section half way through the simulated brain phantom. The concentration procedure is applied dimension by dimension (25) to determine the neighborhoods of the discontinuities. The result is depicted in figure 19 for the $[x, 0]$ cross section, where it is evident that the nonlinear enhancement and minimization procedures described in §V are necessary to pinpoint the edges.

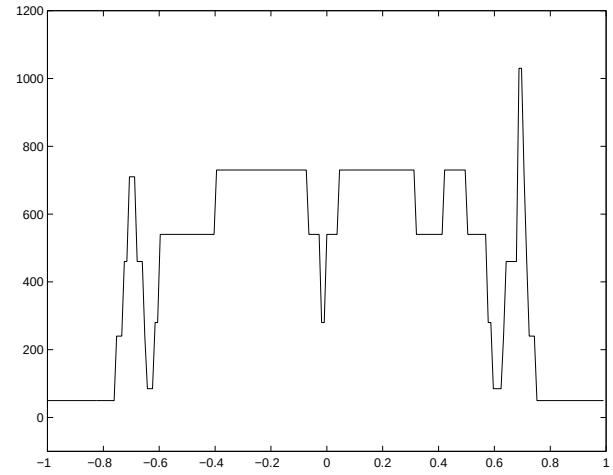

Fig. 18. (a) Cross section of the simulated brain phantom at $[x, 0]$.

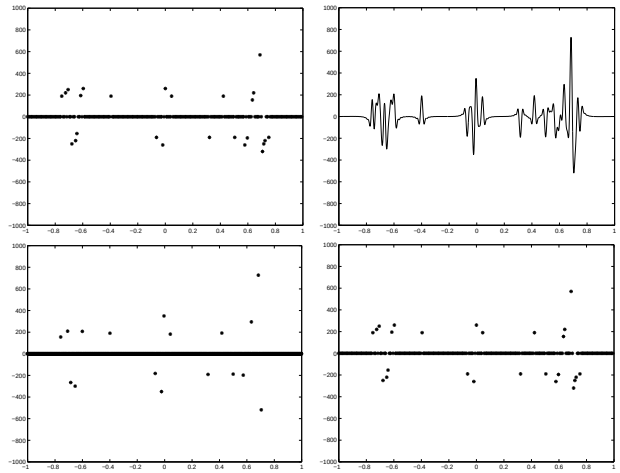

Fig. 19. (a) Jump function of the cross section of the simulated brain phantom at $[x, 0]$ and the performances of (b) the concentration, (c) nonlinear enhancement, and (d) the minimization procedures.

In neuro-imaging, the important structures are all within the skull. With this in mind, it is more efficient to reconstruct the image only within the interior of skull. The boundary detection method described in §V, with the final result displayed in figure 20, allows us to determine the edges of the skull and eliminate unnecessary computing outside the region. It is possible to determine this region due to the fact that the boundary jump between skull and CSF is large relative to other boundaries in a T2 weighted image. We note that the detection of the inside of the brain is still completely automated. Figure 21 depicts the final boundary detection of simulated brain phantom. The results of applying the hybrid Gegenbauer reconstruction method described in §VII to the simulated brain phantom are shown in figures 22 and 23, where it is clear that this reconstructed image is much better than the traditional

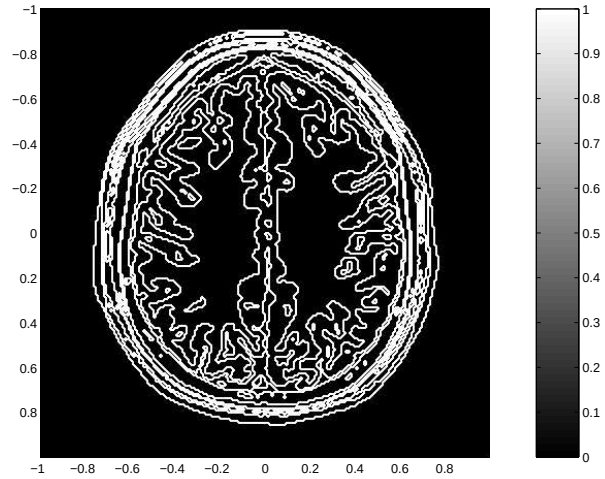

Fig. 20. Final boundary detection of the simulated brain phantom.

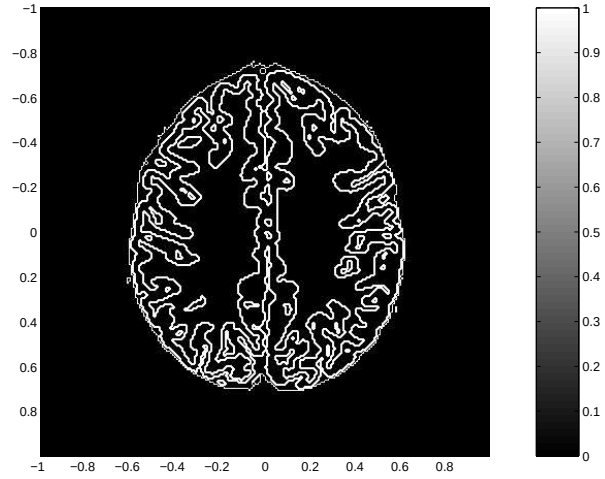

Fig. 21. Skull and CSF boundary detection of the simulated brain phantom.

filtered Fourier reconstruction.

IX. Conclusion

It is possible to improve the accuracy of reconstruction in magnetic resonance imaging by using the edge detection algorithm and hybrid Gegenbauer method. The improvement is significant and specifically excels at maintaining integrity near tissue boundaries. Since it is possible to use FFTs in the Gegenbauer hybrid reconstruction method, the computational cost is not significantly greater than the traditional Fourier filtered reconstruction. The new algorithm described in §V allows us to "pinpoint" all of the boundaries, even if they are located very close together. Furthermore, it gives critical information needed to automatically eliminate the skull.

We note that previous filtering techniques, such as the one described in [2], have been introduced to effectively combat the Gibbs ringing artifact in particular regions of interest. Other Gibbs ringing reducing techniques use image expansion in particular regions of interest. One such recently developed method involves a Bayesian approach that uses a nonlinear image expansion technique to preserve the discontinuities of the original image [19]. The Gegenbauer reconstruction method may have several ad-

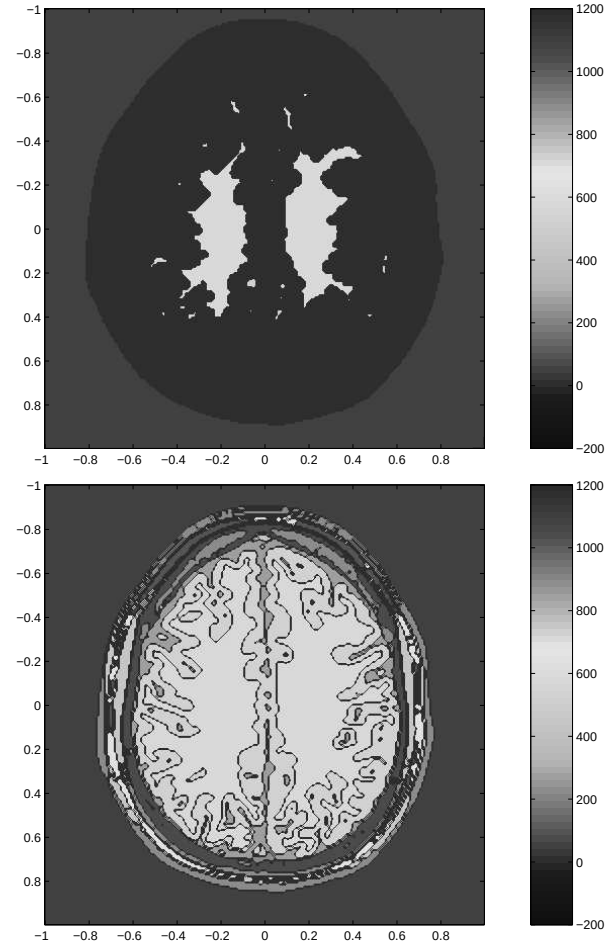

Fig. 22. (a) Filtered Fourier Reconstruction away from the boundaries with $p = 4$ and (b) Gegenbauer reconstruction close to boundaries with $m = \lambda = 4$.

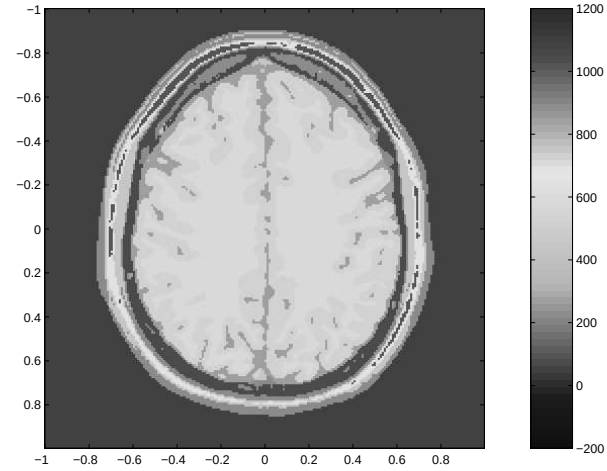

Fig. 23. Final hybrid Gegenbauer reconstruction of the brain phantom.

vantages over these mentioned techniques. In particular, no information is required about the relative expected local signal strength, although such information would enhance the capabilities of the Gegenbauer reconstruction performance since the number of Gegenbauer polynomials required for reconstruction can then be explicitly determined. In comparison to the Bayesian approach, the Gegenbauer method does not require the expensive minimization computations described in [19]. Direct comparisons of these different techniques will be the topic of future work.

Our results in this paper serve as a possible way to improve medical imaging for the MRI. This work has sparked several future considerations.

1. *The development of an optimal minimization procedure.* As repeatedly shown, edge detection provides an essential step in high resolution reconstruction. The new algorithm designed in §V enables higher accuracy reconstruction because of its ability to find very closely placed edges. This minimization procedure should be investigated to optimize computational cost, and will be a subject of future work.
2. *Implementation of the edge detection and reconstruction procedures when noise is present.* It is critical to determine the robustness of these methods when in the presence of realistic noise. Recovery of images from noisy MRI data was addressed in [1], which required the expansion of techniques and theory described here. It was demonstrated that this method is feasible in practical applications, and the techniques presented here are currently being applied to experimental MRI data.
3. *Application to other medical imaging problems.* In our current investigation we assumed k-space data information is given rectilinearly. An adaptation to radially sampled data must be readily available for this method to be applicable to PET imaging problems and/or spiral scanning in MRI.

Appendix

I. Shepp-Logan Phantom Algorithm

$z = 0$

if $(\frac{x}{.69})^2 + (\frac{y}{.92})^2 \leq 1$
then $z = 2$

if $(\frac{x}{.06624})^2 + (\frac{y+.0184}{.874})^2 \leq 1$
then $z = z - .98$

$\xi = (x - .22) \cdot cos(.4\pi) + y \cdot sin(.4\pi)$
$\eta = -(x - .22) \cdot sin(.4\pi) + y \cdot cos(.4\pi)$

if $(\frac{\xi}{.31})^2 + (\frac{\eta}{.11})^2 \leq 1$
then $z = z - .02$

$\xi = (x + .22) \cdot cos(.6\pi) + y \cdot sin(.6\pi)$
$\eta = -(x + .22) \cdot sin(.6\pi) + y \cdot cos(.6\pi)$

if $(\frac{\xi}{.41})^2 + (\frac{\eta}{.16})^2 \leq 1$
then $z = z - .02$

if $(\frac{x-.35}{.3})^2 + (\frac{y}{.6})^2 \leq 1$
then $z = z + 300$

if $(\frac{x}{.21})^2 + (\frac{y-.35}{.25})^2 \leq 1$
then $z = z + .01$

if $(\frac{x}{.046})^2 + (\frac{y-.1}{.046})^2 \leq 1$
then $z = z + .01$

if $(\frac{x}{.046})^2 + (\frac{y+.1}{.046})^2 \leq 1$
then $z = z + .01$

if $(\frac{x+.08}{.046})^2 + (\frac{y+.605}{.023})^2 \leq 1$
then $z = z + .01$

if $(\frac{x}{.023})^2 + (\frac{y+.605}{.023})^2 \leq 1$
then $z = z + .01$

if $(\frac{x-.06}{.023})^2 + (\frac{y+.605}{.023})^2 \leq 1$
then $z = z + .01$

$f(x, y) = z$

Acknowledgments

The work of these authors was supported in part by the Sloan Foundation (A. Gelb), the Arizona Center for Alzheimer's Disease Research (R. Archibald and A. Gelb), NSF grant No DMS01-07428 (A. Gelb), and the Center for System Science and Engineering Research at Arizona State University (R. Archibald and A. Gelb).

References

[1] R. Archibald and A. Gelb, "Reducing the Effects of Noise in Boundary Detection," to appear in *Journal of Scientific Computing*, 2002.
[2] T. Bakir and S.J. Reeves, "A Filter Design Method for Minimizing Ringing in a Region of Interest in MR Spectroscopic Images," *IEEE Transactions on Medical Imaging*, vol. 19, no. 6, pp. 585-600, June 2000.
[3] H. Bateman, *Higher Transcendental Functions, Vol.2*, McGraw-Hill, New York, 1953.
[4] C.A. Cocosco, V. Kollokian, R.K.-S. Kwan, and A.C. Evans, "BrainWeb: Online Interface to a 3D MRI Simulated Brain Database," *NeuroImage*, vol.5, no.4, part 2/4, S425, 1997 – Proceedings of 3-rd International Conference on Functional Mapping of the Human Brain, Copenhagen, May 1997.
[5] D.L. Collins, A.P. Zijdenbos, V. Kollokian, J.G. Sled, N.J. Kabani, C.J. Holmes, and A.C. Evans, "Design and Construction of a Realistic Digital Brain Phantom," *IEEE Transactions on Medical Imaging*, vol. 17, no. 3, pp.463-468, June 1998.
[6] D. Dowsett, P. Kenny, and R. Johnson, *The Physics of Diagnostic Imaging*, Chapman and Hall Medical, 1998.
[7] A. Gelb, "A Hybrid Approach to Spectral Reconstruction of Piecewise Smooth Functions," *Journal of Scientific Computing*, vol. 15, pp. 293-322, 2001.
[8] A. Gelb and D. Gottlieb, "The Resolution of the Gibbs Phenomenon for "Spliced" Functions in One and Two Dimensions," *Computers Math. Applic*, vol. 33, no. 11, pp. 35-58, 1997.
[9] A. Gelb and E. Tadmor, "Detection of Edges in Spectral Data," *Applied and Computational Harmonic Analysis,* vol. 7, pp. 101-135, 1999.
[10] A. Gelb and E. Tadmor, "Detection of Edges in Spectral Data II: Nonlinear Enhancement," *SIAM J. Numer. Anal.,* vol. 38, pp. 1389-1408, 2000.
[11] A. Gelb and E. Tadmor, "Spectral Reconstruction of Piecewise Smooth Functions from Their Discrete Data," to appear in *Mathematical Modelling and Numerical Analysis,* 2002.

[12] D. Gottlieb, B. Gustafsson and Patrik Forssen, "On the Direct Fourier Method for Computer Tomography," *IEEE Transactions of Medical Imaging*, vol. 19, no.3, pp. 223 - 233, 2000.
[13] D. Gottlieb and S. Orszag, *Numerical Analysis of Spectral Methods: Theory and Applications,* SIAM, Philadelphia, 1977.
[14] D. Gottlieb and C-W. Shu, "On the Gibbs Phenomenon and its Resolution," *SIAM Review,* vol. 39, pp. 644-668, 1997.
[15] D. Gottlieb, C-W. Shu, A. Solomonoff, and H. Vandeven, "On the Gibbs Phenomenon I: Recovering Exponential Accuracy From the Fourier Partial Sum of a Nonperiodic Analytic Function," *J. of Comp. and Appl. Math.*, vol. 43, pp. 81-98, 1992.
[16] http://www.bic.mni.mcgill.ca/brainweb/
[17] R.K.-S. Kwan, A.C. Evans, and G.B. Pike: "An Extensible MRI Simulator for Post-Processing Evaluation," *Lecture Notes in Computer Science,* Visualization in Biomedical Computing, Springer-Verlag, vol. 1131, pp. 135-140, 1996.
[18] Z. Liang and P. Lauterbur, *Principles of Magnetic Resonance Imaging, a Signal Processing Perspective*, IEEE Press, 2000.
[19] R.R. Schultz and R.L. Stevenson, "A Bayesian Approach to Image Expansion for Improved Definition," *IEEE Transactions on Image Processing*, vol. 3, no. 3, pp. 233-242, May 1994.